

A complex-valued resonance model for axisymmetric screech tones in supersonic jets

Matteo Mancinelli¹†, Vincent Jaunet¹, Peter Jordan¹, and Aaron Towne²

¹Département Fluides Thermique et Combustion, Institut Pprime - CNRS-Université de Poitiers-ENSMA, 11 Boulevard Marie et Pierre Curie, 86962 Chasseneuil-du-Poitou, Poitiers, France

²Department of Mechanical Engineering, University of Michigan, 2350 Hayward Street, Ann Arbor, MI 48109, USA

(Received xx; revised xx; accepted xx)

We consider the resonance mechanism underpinning generation of A1 and A2 screech tones in an under-expanded supersonic jet. Starting from the resonance model recently proposed by Mancinelli *et al.* (2019a), where the upstream-travelling wave is a neutrally-stable, guided jet mode, we here present a more complete linear-stability-based model for screech prediction. We study temperature and shear-layer thickness effects and show that, in order to accurately describe the experimental data, the effect of the finite thickness of the shear layer has to be incorporated in the jet-dynamics model. We then present an improved resonance model for screech-frequency predictions in which both downstream- and upstream-travelling waves may have complex wavenumber and frequency. This resonance model requires knowledge of the reflection coefficients at the upstream and downstream locations of the resonance loop. We explore the effect of the reflection coefficients on the resonance model and propose an approach for their identification. The complex-mode model allows to identify frequency-flow regions of positive values of the frequency imaginary part for which the resonance loop is amplified in time and resonance is sustained and is finally found to provide the most complete description of the measured data.

Key words: Authors should not enter keywords on the manuscript, as these must be chosen by the author during the online submission process and will then be added during the typesetting process (see <http://journals.cambridge.org/data/relatedlink/jfm-keywords.pdf> for the full list)

1. Introduction

The modelling of screech in imperfectly expanded supersonic jets is a long-standing problem to which a large body of work has been devoted (for a comprehensive review on the subject see Raman (1999) and Edgington-Mitchell (2019)).

It is known that screech is driven by resonance associated with a feedback loop involving a downstream-travelling flow disturbance generated at the nozzle exit and an upstream-travelling wave generated by the interaction of the flow disturbance with the shock cells. Since the work of Powell (1953), it has been assumed that the closure

† Email address for correspondence: matteo.mancinelli@univ-poitiers.fr

mechanism is provided by upstream-travelling free-stream acoustic waves. On the basis of this phenomenological description, several screech-frequency prediction models have been proposed (Powell 1953; Tam *et al.* 1986; Panda 1999; Gao & Li 2010). These provide only rough agreement with experimental data, and many screech features, such as staging, are not satisfactorily captured.

As shown by Powell *et al.* (1992), the staging evolution of the screech frequency with jet Mach number is characterised by switching between modes or stages: axisymmetric A1 and A2 modes (Merle 1957), flapping B and D modes (Mercier *et al.* 2017) and helical C mode (Edgington-Mitchell *et al.* 2014). The idea that screech may not be closed by free-stream acoustic waves was first suggested by Shen & Tam (2002), who claimed that A1 and B screech modes involve free-stream acoustic waves, whereas A2 and C modes involve upstream-travelling guided jet modes. These guided modes were first studied by Tam & Hu (1989) and have since been used to explain many resonance phenomena: in subsonic and supersonic impinging jets (Tam & Ahuja 1990; Bogey & Gojon 2017), in high-speed subsonic jets (Towne *et al.* 2017) and in a jet-flap interaction configuration (Jordan *et al.* 2018). Most importantly, they have been shown to be active in screeching supersonic jets (Edgington-Mitchell *et al.* 2018; Gojon *et al.* 2018). Given this observation, we recently developed a screech-frequency prediction model based on a resonance between downstream-travelling Kelvin-Helmholtz (K-H) waves and upstream-travelling guided jet modes (Mancinelli *et al.* 2019a). The phase speeds of both the K-H and upstream-travelling jet waves were provided by a cylindrical vortex-sheet (V-S) model. Contrary to the assertion of Shen & Tam (2002), the study showed that both A1 and A2 screech modes are underpinned by a resonance involving the upstream-travelling guided jet modes and screech-frequency predictions provided better agreement with experiments than does the classical prediction approach proposed by Powell (1953) using free-stream acoustic waves.

The model of Mancinelli *et al.* (2019a) considers an isothermal jet. We here consider the effect of jet temperature and show that a finite-thickness model is required to capture the temperature effects on screech generation. In the model of Mancinelli *et al.* (2019a), consistent with what is frequently assumed in fluid-mechanics resonance phenomena, both the upstream- and downstream-travelling waves are considered to be spatially neutrally stable. With this assumption, knowledge of the magnitude of the reflection coefficients is not necessary for screech-frequency prediction. While predictions provide good agreement with data, the simplification misses certain aspects of the observed behaviour: the model predicts tones that are not observed experimentally, for instance. This inaccuracy arises for both the free-stream- and guided-jet-mode-based resonance models.

We here explore the limitations of the neutral-mode approach presented in Mancinelli *et al.* (2019a) and consider a more complete model in which both frequency and wavenumber may be complex so that the growth rate of the waves involved in the resonance is included. This requires consideration of the upstream and downstream reflection mechanisms, which take form of a reflection-coefficient product. While the reflection coefficients could be determined by using a Wiener-Hopf method (Noble 1958; Rienstra 2007) or by detailed numerical analysis, we here follow the approach used by Jordan *et al.* (2018) to study resonance in a jet-flap interaction configuration; that is, we treat the reflection-coefficient product as a parameter and explore the predictions obtained by imposing its amplitude and phase. We then consider a simplified real-frequency-based variant of the model to experimentally educe values of the reflection-coefficient product. On the basis of these results, we propose a functional form for the frequency-Mach-number dependence of the reflection-coefficient product. The refined

resonance model, that includes finite-thickness and temperature effects, provides a more complete description of the experimental observations, and, in particular, it removes spurious tone predictions that occur with real-frequency models.

The paper is organised as follows. The resonance model is presented in §2. §3 describes the experimental set-up and instrumentation. Main results concerning the screech-frequency predictions and the estimation of the reflection-coefficient product are reported in §4. Conclusions are finally presented in §5.

2. Resonance models

In this section, we present the model based on a resonance between downstream-travelling K-H instability waves and two kinds of upstream-travelling wave: (i) free-stream acoustic waves, which are used in the usual screech scenario, and (ii) guided jet modes. Following Towne *et al.* (2017) and Mancinelli *et al.* (2019a), we use the terms downstream- and upstream-travelling to designate the sign of the group velocity. Accordingly, the downstream- and upstream-travelling waves are denoted using superscripts + and $-$, respectively. The Kelvin-Helmholtz instability is denoted k_{KH} , the guided jet modes k_p and the free-stream acoustic waves k_a . Modes are provided by linear stability theory.

2.1. Jet models

The jet is modelled using locally-parallel linear stability theory. All variables are normalised by the nozzle diameter D , the ambient density and speed of sound ρ_∞ and c_∞ , respectively. The Reynolds decomposition,

$$q'(x, r, \theta, t) = \bar{q}(r) + q(x, r, \theta, t), \quad (2.1)$$

is applied to the flow-state vector q' , where the mean and fluctuating components are \bar{q} and q , respectively. We assume the normal-mode ansatz,

$$q(x, r, \theta, t) = \hat{q}(r) e^{i(kx + m\theta - \omega t)}, \quad (2.2)$$

where k is the streamwise wavenumber normalised by the nozzle diameter D , m is the azimuthal mode and $\omega = 2\pi St M_a$ is the non-dimensional frequency, where $St = fD/U_j$ is the nozzle-diameter-based Strouhal number and $M_a = U_j/c_\infty$ the acoustic Mach number. As discussed by Towne *et al.* (2017), k_p modes belong to a hierarchical family of waves identified by their azimuthal and radial orders m and n , respectively, and exist as propagative waves only in a well defined St number range (see §2.3). We here restrict attention to azimuthal mode $m = 0$ due to the axisymmetry property of screech modes A1 and A2 and we let the radial order vary in the range $n = 1, 2$ for the frequency range of screech modes of interest.

This theory is applied to two different models: a simplified cylindrical vortex sheet and a finite-thickness flow model. Both are governed by the compressible Linearised Euler Equations (LEE).

2.1.1. Cylindrical vortex-sheet model

Following our previous work (Mancinelli *et al.* 2019a), the linear wave dynamics are first modelled using a cylindrical vortex sheet (Lessen *et al.* 1965; Michalke 1970). The vortex-sheet dispersion relation is,

$$D(k, \omega; M_a, T, m) = \frac{1}{\left(1 - \frac{k M_a}{\omega}\right)^2} + \frac{1}{T} \frac{I_m\left(\frac{\gamma_i}{2}\right) \left(\frac{\gamma_o}{2} K_{m-1}\left(\frac{\gamma_o}{2}\right) + m K_m\left(\frac{\gamma_o}{2}\right)\right)}{K_m\left(\frac{\gamma_o}{2}\right) \left(\frac{\gamma_i}{2} I_{m-1}\left(\frac{\gamma_i}{2}\right) - m I_m\left(\frac{\gamma_i}{2}\right)\right)} = 0, \quad (2.3)$$

with

$$\gamma_i = \sqrt{k^2 - \frac{1}{T} (\omega - M_a k)^2}, \quad (2.4a)$$

$$\gamma_o = \sqrt{k^2 - \omega^2}, \quad (2.4b)$$

where I_m and K_m are modified Bessel functions of the first and second kind, respectively, and $T = T_j/T_\infty$ is the jet-to-ambient temperature ratio. The relation between the acoustic and jet Mach numbers is given by $M_j = U_j/c_j = M_a/\sqrt{T}$. The branch cut of the square root in eqs. (2.4a) and (2.4b) is chosen such that $-\pi/2 \leq \arg(\gamma_{i,o}) \leq \pi/2$.

Frequency/wavenumber pairs (ω, k) that satisfy eq. (2.3) define eigenmodes of the vortex sheet for given values of m , M_a and T . To find these pairs, we specify a frequency ω and compute the associated eigenvalues k for the K-H and guided jet modes according to eq. (2.3). By virtue of the normalisation adopted, the free-stream acoustic waves are simply defined by $k_a^\pm = \pm 2\pi St M_a$.

2.1.2. Finite-thickness flow model

Writing the LEE equations in terms of the pressure, the compressible Rayleigh equation is obtained,

$$\frac{\partial^2 \hat{p}}{\partial r^2} + \left(\frac{1}{r} - \frac{2k}{\bar{u}_x k - \omega} \frac{\partial \bar{u}_x}{\partial r} - \frac{\gamma - 1}{\gamma \bar{\rho}} \frac{\partial \bar{\rho}}{\partial r} + \frac{1}{\gamma T} \frac{\partial \bar{T}}{\partial r} \right) \frac{\partial \hat{p}}{\partial r} - \left(k^2 + \frac{m^2}{r^2} - \frac{(\bar{u}_x k - \omega)^2}{(\gamma - 1) \bar{T}} \right) \hat{p} = 0, \quad (2.5)$$

where γ is the specific heat ratio for a perfect gas. The solution of the linear stability problem is obtained specifying a real or complex frequency ω and solving the resulting augmented eigenvalue problem $k = k(\omega)$, with $\hat{p}(r)$ the associated pressure eigenfunction. The eigenvalue problem is solved numerically by discretizing (2.5) in the radial direction using Chebyshev polynomials. A mapping function is used to non-uniformly distribute the grid points such that they are dense in the region of shear (Trefethen 2000).

With the aim of keeping the model as simple as possible and exploring the shear-layer thickness effect, we here use the hyperbolic-tangent velocity profile (Lesshafft & Huerre 2007),

$$\bar{u}_x(r) = \frac{1}{2} M_a \left(1 + \tanh \left(\frac{R}{4\theta_R} \left(\frac{R}{r} - \frac{r}{R} \right) \right) \right), \quad (2.6)$$

where θ_R is the shear-layer momentum thickness and $R = 0.5$ is the nozzle radius.

Different values of R/θ_R are considered to assess the shear-layer thickness effect on screech generation and, specifically, on the frequency range of existence of propagative guided modes. Consistent with results obtained from experimental Particle Image Velocimetry (PIV) measurements (see §A), we select a shear layer with $R/\theta_R = 10$.

2.2. Resonance conditions

Resonance conditions are obtained by assuming that upstream- and downstream-travelling waves exchange energy at the nozzle exit and at the s -th shock-cell location,

where an interaction between the K-H instability wave and the shock-cell pattern occurs. Following Landau & Lifshitz (1958), the condition to be satisfied for resonance to occur is,

$$R_1 R_2 e^{i \Delta k L_s} = 1, \quad (2.7)$$

where $R_1(St, M_j) \in \mathcal{C}$ and $R_2(St, M_j, L_s) \in \mathcal{C}$ are the reflection coefficients at the nozzle exit and shock-cell location, respectively, $\Delta k = k^+ - k^-$ is the difference between the wavenumbers of the downstream- and upstream-travelling waves and L_s is the distance between the nozzle exit and the s -th shock cell. Following Jordan *et al.* (2018), eq. (2.7) can be re-written in terms of magnitude and phase constraints associated with the imaginary and real parts of the eigenvalues k , respectively,

$$e^{\Delta k_i L_s} = |R_1 R_2|, \quad (2.8a)$$

$$\Delta k_r L_s + \phi = 2p\pi, \quad (2.8b)$$

where Δk_i and Δk_r are the imaginary and real parts of Δk , $\phi = \angle R_1 R_2$ is the phase of the reflection-coefficient product and p is an integer associated with the difference in the number of oscillations between the downstream- and upstream-travelling waves.

Following our previous results (Mancinelli *et al.* 2019a) and in agreement with results reported in the literature (Mercier *et al.* 2017), we consider the fourth shock cell as the downstream reflection point, i.e. $s = 4$. The distance L_s between the nozzle exit and the s -th shock cell is given by

$$L_s(M_j) = L_1((1 - \alpha)s + \alpha), \quad (2.9)$$

where L_1 is the length of the first shock cell and α the rate of decrease of the shock-cell length with the downstream distance, whose value was estimated as 0.06 by Harper-Bourne (1974). The length of the first shock cell can be obtained using the V-S model and by carrying out a zero-frequency analysis. When $\omega \rightarrow 0$ the dispersion relation in (2.3) reduces to

$$I_m\left(\frac{\gamma_i}{2}\right) = 0, \quad (2.10)$$

which, exploiting the properties of the Bessel functions, can be written as,

$$I_m\left(\frac{\gamma_i}{2}\right) = i^{-m} J_m\left(\frac{i\gamma_i}{2}\right) = 0. \quad (2.11)$$

Since we intend to describe the mean-flow shock-cell structure of an axisymmetric jet, we consider $m = 0$. The first zero of the Bessel function J_0 , (2.11) is satisfied when

$$i\frac{\gamma_i}{2} = 2.4048. \quad (2.12)$$

Substituting for γ_i (2.4a) in (2.12), we obtain the Prandtl-Pack model (Pack 1950) for the length of the first shock cell,

$$L_1(M_j) = \frac{\pi}{2.4048} \sqrt{M_j^2 - 1}. \quad (2.13)$$

The reflection coefficients R_1 and R_2 are unknown functions of frequency and flow conditions. Two modelling approaches may be pursued in which the frequency, ω , is either real or complex, and in each approach the reflection-coefficient product is handled

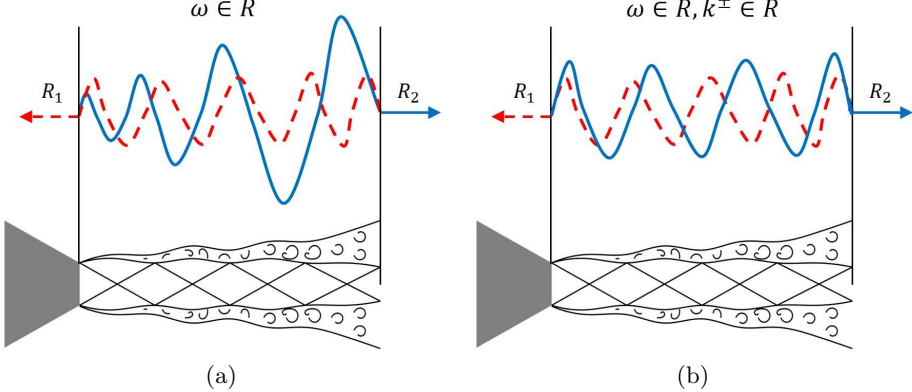


FIGURE 1. Schematic representation of the resonance loop: (a) real-frequency analysis, (b) neutral-mode model. Solid blue and dashed red lines refer to downstream- and upstream-travelling waves, respectively.

differently. Following Mancinelli *et al.* (2019a), we first use the real-frequency analysis to show that the feedback process in the generation of A1 and A2 screech modes is underpinned by guided jet modes rather than free-stream acoustic waves considered in the closure mechanism proposed by Powell (1953) and most other studies since. We then explore both temperature and shear-layer thickness effects on screech. This allows us to identify the limitations of real-frequency-based models and explore improvements that may be obtained using the complex-frequency model.

2.3. Neutral-mode model

If the frequency is considered real, resonance involves a spatially-unstable downstream-travelling K-H mode and a neutrally-stable upstream-travelling wave: $\omega \in \mathcal{R}$, $k^+ \in \mathcal{C}$, and $k^- \in \mathcal{R}$. The reflection coefficients R_1 and R_2 at the nozzle exit and shock-cell location, respectively, are such that resonance involves tones that neither grow nor decay in time. A schematic depiction of this scenario is provided in figure 1(a).

A further widely used simplification involves assuming that both the downstream- and upstream-travelling waves are neutrally stable: $k^+ \in \mathcal{R}$ and $k^- \in \mathcal{R}$ (see schematic representation in figure 1(b)). Since Δk_i is then identically zero, this allows us to neglect the magnitude constraint of eq. (2.8a). Resonance-frequency prediction can be obtained either from the dispersion relation (2.3) or from the Rayleigh equation (2.5) by specifying real values of ω , computing k and then imposing the phase constraint (2.8b) to obtain the resonance frequency. Given that the phase of the reflection-coefficient product is an unknown, we follow Jordan *et al.* (2018) and Mancinelli *et al.* (2019a) by exploring

different phase values: $\phi = 0, -\pi/4, -\pi/2$ and $-\pi$, which lead to the following resonance criteria,

$$\phi = 0 \implies \operatorname{Re} [k^+ - k^-] = \Delta k_r = \frac{2p\pi}{L_s}, \quad (2.14a)$$

$$\phi = -\pi/4 \implies \operatorname{Re} [k^+ - k^-] = \Delta k_r = \frac{(2p + 1/4)\pi}{L_s}, \quad (2.14b)$$

$$\phi = -\pi/2 \implies \operatorname{Re} [k^+ - k^-] = \Delta k_r = \frac{(2p + 1/2)\pi}{L_s}, \quad (2.14c)$$

$$\phi = -\pi \implies \operatorname{Re} [k^+ - k^-] = \Delta k_r = \frac{(2p + 1)\pi}{L_s}. \quad (2.14d)$$

Predictions obtained using $\phi = -\pi/4$ (2.14b) and in-phase reflection conditions (2.14a) provide best agreement with the experimental data when using the vortex-sheet and finite-thickness dispersion relations, respectively. This discrepancy in phase between the two flow models is expected since the phase speed of the K-H mode changes significantly between the vortex sheet and the finite-thickness model (Michalke 1984).

Figure 2(a) shows the eigenvalue trajectories for azimuthal mode $m = 0$, as a function of frequency, in the k_r - k_i and k_r - St planes for the V-S dispersion relation. Shown are the trajectories of the K-H and guided jet modes, and of the downstream- and upstream-travelling free-stream acoustic waves. The flow considered is cold and fully expanded, with temperature ratio $T = T_j/T_\infty \approx 0.81$ and jet Mach number $M_j = 1.08$. A non-dispersive wave with a phase speed equal to $0.8 U_j$ frequently adopted to approximate the K-H mode (Schmidt *et al.* 2017) has been added to the plot. We note that k_{KH} is slightly dispersive with phase speed greater than the usually adopted value of $0.8 U_j$ as shown by the comparison with the constant phase speed line, $St = (0.8U_j)k$. We note the following features for the guided jet modes. They are characterised by a negative phase speed and, following Towne *et al.* (2017), we distinguish between guided jet modes with positive and negative group velocities. Only the k_p^- modes may close the resonance loop. Unlike free-stream sound waves, they are dispersive, with subsonic phase speed very close to the value of the ambient speed of sound, particularly in the low-frequency part of the branch. They furthermore exist as propagative waves only in a well-defined Strouhal number range delimited by the branch and saddle points, $B(m, n)$ and $S(m, n)$, respectively (Tam & Hu 1989). Outside this frequency band, the guided modes are evanescent and therefore not included in the modelling. For the first radial order the branch point coincides with the origin in the k_r - St plane (Tam & Ahuja 1990).

The trajectories of the K-H and guided jet modes using the finite-thickness dispersion relation with $R/\theta_R = 10$ for the same flow conditions considered above are shown in figure 2(b). Among the guided modes, only the eigenvalues of k_p^- modes are reported for the sake of brevity. The k_{KH} wave shows a higher dispersive nature with a much lower phase speed than that computed using the vortex sheet, as discussed above. We also note that, contrary to the VS, the amplitude of the growth rate of the k_{KH} mode is not monotonically increasing with the frequency.

Figure 3 shows the resonance frequency selection in the case of a resonance between k_{KH}^+ and k_p^- modes of first and second radial orders for azimuthal mode $m = 0$, $M_j = 1.08$, $T_j/T_\infty \approx 0.81$ and in-phase reflection conditions. For the sake of brevity, we only report the results obtained using the finite-thickness dispersion relation. Resonance can only exist in a frequency range where both downstream- and upstream-travelling waves exist and are propagative. It is thus clear that, when k_p^- modes are considered, eligible

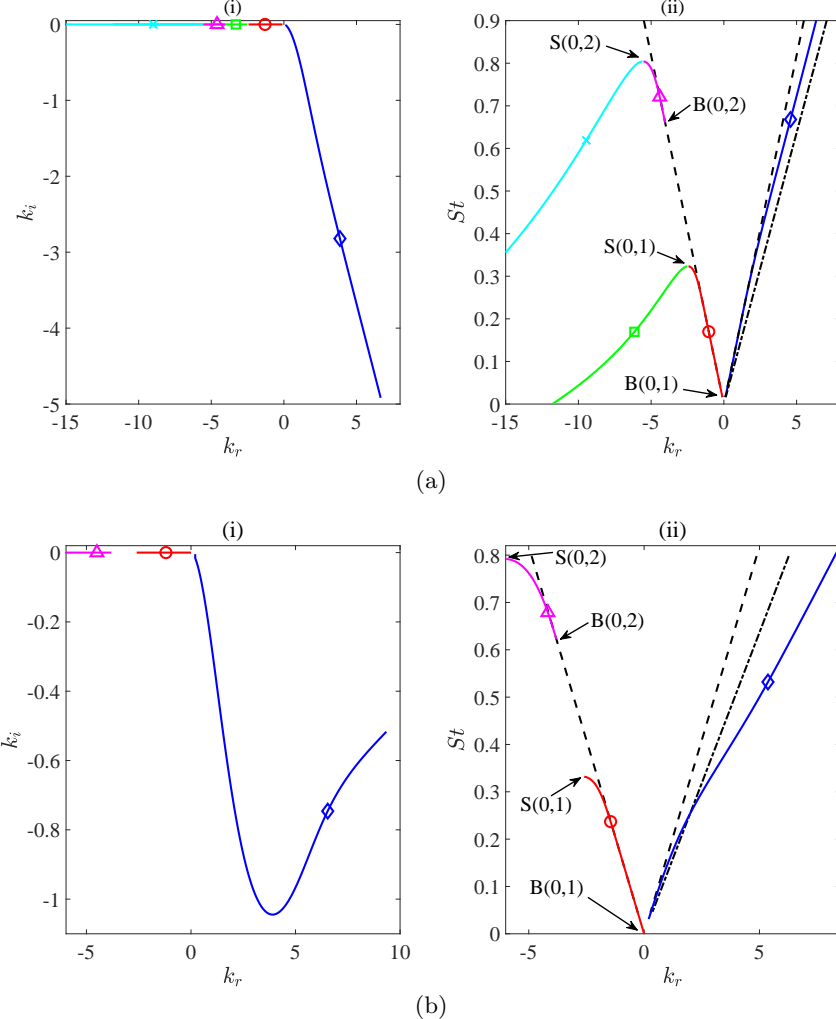


FIGURE 2. Eigenvalues of k_{KH}^+ , k_p^\pm and k_a^\pm in the case of a real-frequency analysis for azimuthal mode $m = 0$, cold jet and fully expanded jet Mach number $M_j = 1.08$: (a) vortex-sheet model, (b) finite-thickness model with $R/\theta_R = 10$; (i) k_r - k_i plane, (ii) k_r - St plane. blue \diamond corresponds to k_{KH}^+ , red \circ to k_p^- for $n = 1$, green \square to k_p^+ for $n = 1$, magenta \triangle to k_p^- for $n = 2$, cyan \times to k_p^+ for $n = 2$, dash-dotted black line to a non-dispersive approximation of K-H mode whose phase speed is $0.8 U_j$, dashed black lines to k_a^\pm . The branch and saddle points of the guided jet modes for each pair of (m, n) orders are indicated with letters B and S , respectively.

resonance frequencies lie in the band delimited by the branch and saddle points. The resonance frequency is found by imposing the phase constraint, which implies computing the intersection between the Δk_r and the value on the right hand-side of the equation of the in-phase resonance criterion (2.14a).

2.4. Complex-mode model

In the complex-frequency analysis both k^+ and $k^- \in \mathcal{C}$. The screech loop involves an unstable downstream-travelling K-H mode and an evanescent upstream-travelling wave. The complex-frequency analysis provides, as additional result, information on the

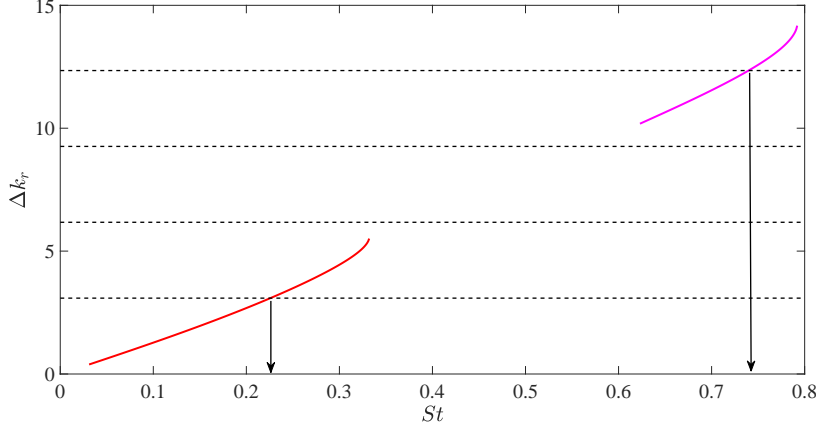


FIGURE 3. Δk_r between k_{KH}^+ and k_p^- modes computed using the finite-thickness model and identification of the resonance frequency in the case of neutral-mode assumption for azimuthal mode $m = 0$, $M_j = 1.08$ and $T \approx 0.81$. Solid red line refers to k_p^- for $n = 1$, dash-dotted magenta line to k_p^- for $n = 2$, horizontal dashed black lines to resonance criteria in the case of in-phase reflection conditions (2.14a).

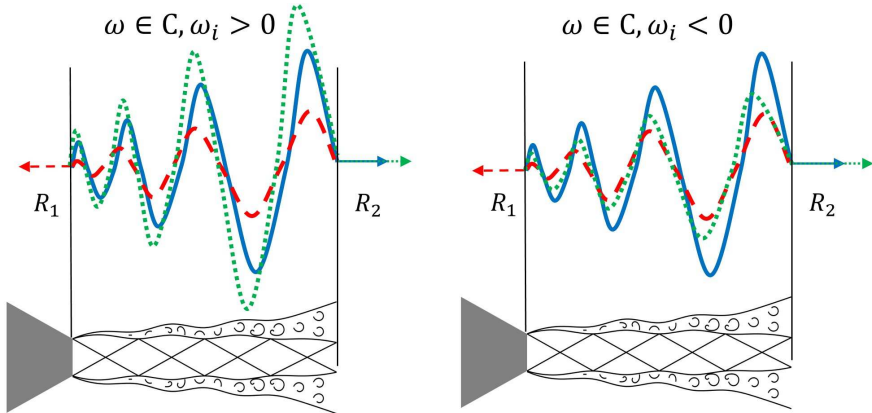


FIGURE 4. Schematic representation of the resonance loop in the complex-frequency analysis. Solid blue lines refer to the downstream-travelling wave, dashed red lines to the upstream-travelling wave and dash-dotted green lines to the fed downstream-travelling wave in a new cycle of the resonance loop.

temporal amplification of the resonance loop: for positive values of the imaginary part of the frequency the screech loop is amplified in time and resonance is sustained; for $\omega_i < 0$ the screech loop is attenuated in time and resonance is damped. A schematic depiction of these scenarios is provided in figure 4.

Resonance-frequency prediction involves finding triplets $[k^+, k^-, \omega] \in \mathcal{C}$ simultaneously satisfying either the dispersion relation (2.3) or the Rayleigh equation (2.5) and both the magnitude and phase constraints (2.8a) and (2.8b), respectively. This implies knowledge of the reflection-coefficient product $R_1 R_2$ as a function of frequency and jet Mach number. As this function is unknown, we first use the reflection-coefficient product as a parameter with a prescribed amplitude. We then identify a frequency-Mach-number-dependent model for the reflection-coefficient product. Prediction involves solving eqs. (2.3) or (2.5)

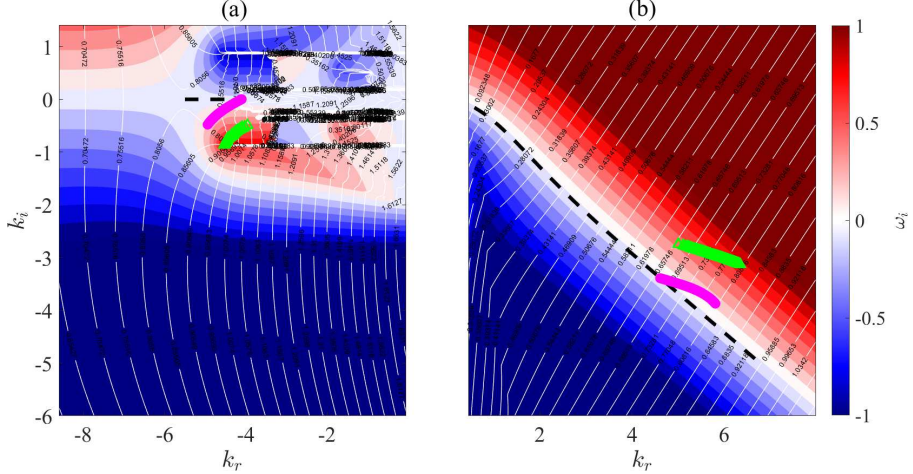


FIGURE 5. Vortex-sheet solutions satisfying eq. (2.3) in the case of complex-frequency analysis for azimuthal mode $m = 0$, fully expanded jet Mach number $M_j = 1.08$ and $T \approx 0.81$ for: (a) k_p^- for $n = 2$, (b) k_{KH}^+ . The colour map shows ω_i , whereas the white contour represents $St = \omega_r / 2\pi M_a$. Dashed black lines represent the eigenvalues in the case of real-frequency analysis. Markers represent eigenvalues satisfying both the dispersion relation (2.3) and the magnitude constraint (2.8a) for $s = 4$ and different values of $|R_1 R_2|$: magenta \circ to $|R_1 R_2| = 10^{-3}$, green \triangle to $|R_1 R_2| = 10^{-2}$.

and (2.8a) to find complex frequencies and eigenvalues that satisfy both the vortex-sheet dispersion relation or the Rayleigh equation and the magnitude constraint. The phase constraint (2.8b) is then used to select resonance frequencies.

For the following discussion, we consider the eigenspectrum of the vortex sheet. This allows us to highlight certain features of the complex-mode model in comparison to the neutral-mode one. However, the complex-mode resonance conditions are used after to compute resonance frequency using the finite-thickness dispersion relation. Figure 5 shows the vortex-sheet solutions $\omega(k)$ for k_{KH}^+ and k_p^- modes of second radial order for azimuthal mode $m = 0$, Mach number $M_j = 1.08$, $T \approx 0.81$ and with the fourth shock-cell location taken as downstream reflection point. Eigenvalues obtained from both real- and complex-frequency analyses are represented. Eigenvalues for $\omega \in \mathcal{C}$ are computed for two values of the reflection-coefficient product amplitude: $|R_1 R_2| = 10^{-3}$ and 10^{-2} . As pointed out above, both downstream- and upstream-travelling waves are characterised by $k_i < 0$ for $\omega \in \mathcal{C}$, implying that k_{KH}^+ and k_p^- are, respectively, spatially unstable and spatially evanescent. Consistent with sustained resonance, the eigenvalues for $\omega \in \mathcal{C}$ move in the $k_r - k_i$ plane towards regions of positive imaginary frequency. Specifically, for a given value of the reflection-coefficient product, only $\omega_i \geq 0$ satisfies the amplitude condition in (2.8a). This feature of the complex-mode model allows us to identify frequency-Mach number combinations for which resonance is sustained.

Figure 6 illustrates the resonance-frequency selection when $\omega \in \mathcal{C}$ for azimuthal mode $m = 0$, $M_j = 1.08$ and $T \approx 0.81$. Consistent with what was found using finite-thickness neutral-mode model, best agreement is observed for in-phase reflection conditions (2.14a). In what follows we compare predictions with experiments.

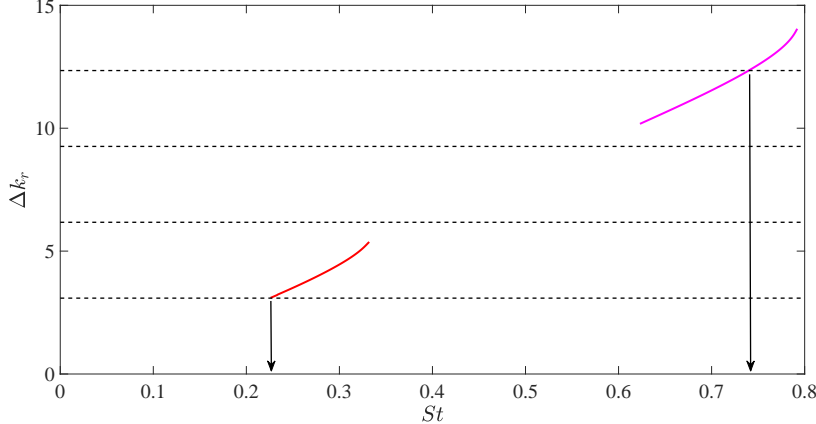


FIGURE 6. Δk_r between k_{KH}^+ and k_p^- modes computed using the finite-thickness model and identification of the resonance frequency in the case of complex frequency for azimuthal mode $m = 0$, $M_j = 1.08$, $T \neq 1$ and magnitude of the reflection-coefficient product $|R_1 R_2| = 0.3$. Solid red line refers to k_p^- for $n = 1$, dash-dotted magenta line to k_p^- for $n = 2$, horizontal dashed black lines to in-phase resonance criteria (2.14a).

3. Experimental set-up

The experimental test campaign was performed at the *SUCRÉ* (SUPersoniC REsonance) jet-noise facility of the *Prométee* technological platform of the *Institut Pprime* in Poitiers. The supersonic under-expanded jet issues from a simple convergent nozzle of diameter $D = 10\text{mm}$ and nozzle-lip thickness of 0.3mm . Experimental tests were carried out for a stagnation pressure range $p_0 = [1.89, 5.75] \cdot 10^5 \text{ Pa}$ with a corresponding fully expanded jet Mach number range $M_j = [1, 1.8]$ and a nozzle diameter-based Reynolds number range $Re = U_j D / \nu = [2.86 \cdot 10^5, 7.9 \cdot 10^5]$. The jet facility includes a heating system to maintain a constant stagnation temperature $T_0 = 295\text{K}$. Fully-expanded conditions at the nozzle exit are computed from the stagnation conditions using the isentropic relations. The tests were performed with a very fine resolution $\Delta M_j = 0.005$ for $M_j = [1, 1.3]$ in order to capture the fine details of the Mach-number dependence of screech modes A1 and A2, and with a resolution $\Delta M_j = 0.01$ for $M_j = [1.31, 1.8]$.

Acoustic and PIV measurements were carried out to investigate the near-pressure and velocity fields, respectively.

3.1. Acoustic measurements

Pressure fluctuations were measured by GRAS 46BP microphones, whose frequency response is flat in the range 4 Hz - 70 kHz . Data were acquired by a National Instruments PXIe-1071 acquisition card with a sampling frequency of 200 kHz which provides a maximum resolved Strouhal number range $[2, 3.2]$ well above the St of interest in this paper. The acquisition time was set equal to 30 s , which is six orders of magnitude larger than the longest convective time, thus ensuring statistical convergence of the quantities presented in the paper. An azimuthal array of six microphones was placed in the nozzle exit at a radial distance $r/D = 1$ from the jet centreline. It was thus possible to resolve the most energetic azimuthal Fourier modes: $m = 0, \pm 1, \pm 2$. The accuracy of the azimuthal Fourier decomposition at the tone frequencies was checked by computing the coherence between neighbouring microphones (Cavalieri *et al.* 2012). Additional details on the jet

facility and a schematic depiction of the experimental set-up and microphone disposition can be found in Mancinelli *et al.* (2019a) and Mancinelli *et al.* (2019b).

3.2. Particle Image Velocimetry measurements

PIV measurements were performed for several jet Mach numbers $M_j = 1.08, 1.12, 1.16, 1.22, 1.3, 1.43, 1.47$ and 1.55 in order to provide a description of the mean flow to inform the finite-thickness model (see §2.1.2 and §A). The flow was seeded using ordinary oil particles before entering the stagnation chamber ensuring seeding homogeneity. The particles were illuminated by a $2 \times 200\text{ mJ}$ Nd-YAG laser and the images were recorded with a 4 Mpix CCD camera equipped with a Sigma DG Macro 105 mm allowing the measurement of the jet up to $x/D = 10$ in the downstream direction. The PIV image pairs were acquired at a sampling rate of 7.2 Hz with a Δt of $1\mu\text{s}$. For each configuration a total of 10000 image pairs were acquired in order to obtain well converged statistics. The images were processed using LaVision's Davis 8.0 software using a multi-pass iterative correlation algorithm (Willert & Gharib 1991; Soria 1996) starting with interrogation area of 64×64 pixels and finishing by 16×16 pixels with deforming windows. The overlap between neighbouring interrogation windows was 50%, leading to a resolution of about 2.375 vectors per millimeter (i.e. 55 vectors per jet diameter) in the measured field. At each correlation pass, a peak validation criterion was used: vectors were rejected if the correlation peak was lower than 0.3. This value was selected as the minimum acceptable value ensuring validation in the potential regions of the flow while rejecting most of the evident erroneous vectors. Outliers were then further detected and replaced using universal outlier detection (Westerweel & Scarano 2005). Main results of PIV measurements are given in §A.

4. Results

Figure 7 shows the Power Spectral Density (PSD) in dB/St as a function of St and M_j for azimuthal mode $m = 0$. The PSD was computed using Welch's method (Welch 1967) with a Strouhal-number resolution $[1, 1.5] \cdot 10^{-3}$. The screech modes A1 and A2 are detected in the jet Mach number range $[1.07, 1.23]$. A weaker low-frequency peak, which we hereinafter denote TM, is also detected for all Mach numbers. We furthermore detect the signature of asymmetric B, C and D modes in the mid-frequency range and of their harmonics for higher frequencies. We finally note that a weak signature of the U mode is detected just above the C mode. This screech stage was also observed by Powell *et al.* (1992) who speculated that it is the extension of the A2 mode. We show in §B that the appearance of B, C and D modes in the PSD map of the axisymmetric component of the pressure is due to non-linear interaction between azimuthal modes $m = +1$ and $m = -1$. Our focus in what follows is the modelling of axisymmetric screech modes A1, A2 and TM.

4.1. Neutral-mode analysis

4.1.1. Vortex-sheet model

Figure 8 shows the PSD map for $m = 0$ and resonance-frequency predictions obtained using the neutral-mode analysis and considering both free-stream acoustic waves and guided jet modes. The branch- and saddle-point tracks are also shown. Predictions are computed using the vortex sheet to describe the jet-wave dynamics and considering a cold jet. We point out that the jet-to-ambient temperature ratio $T = T_j/T_\infty$ varies with M_j in the range $\approx [0.61, 0.83]$. As outlined in §2.3, best predictions are obtained in this

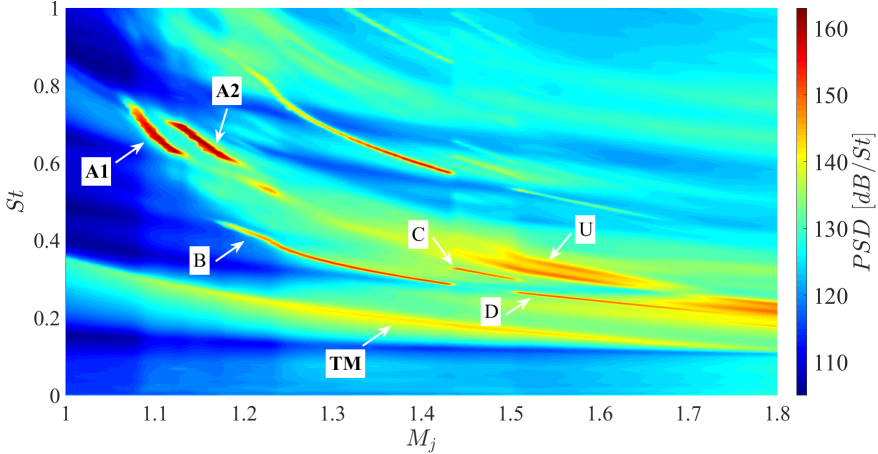


FIGURE 7. PSD map of mode $m = 0$ and detection of tones of interest. Tones of interest, i.e. A1, A2 and TM, are labelled in bold.

case imposing $\phi = -\pi/4$ as reflection condition (2.14d), where we let the integer p vary in the range $p = 1, \dots, 7$. Predictions for TM, A1 and A2 screech modes are obtained for values of p equal to 2, 3 and 4, respectively. A summary of the parameters used to obtain predictions is reported in table 1. We point out that, where guided-mode predictions are concerned, A1 and A2 screech modes are associated with guided modes of second radial order ($n = 2$), whereas the TM mode is due to guided modes of first radial order ($n = 1$). We note that cut-on and cut-off frequencies of screech tones are not captured by the free-stream-acoustic-wave-based resonance model which predict resonance frequencies for regions where no tones are measured. In contrast, the guided-mode-based model roughly captures the cut-on and cut-off screech frequencies through the definition of a M_j - St region of eligible resonance frequencies delimited by the branch- and saddle-point tracks. Although much more accurate than the model based on k_a^- waves, the guided-mode-based model shows a rough agreement with experimental data. Specifically, the low-frequency part of A1 and, above all, A2 modes is cut out of the St -band of existence of propagative k_p^- modes and hence cannot be predicted by the model. We underline that the better agreement with experiments observed in Mancinelli *et al.* (2019a) is, indeed, related to the fact that we considered an isothermal jet in that work. As we show later, the good description of the experimental data that we achieve by considering a more realistic cold jet with finite thickness of the shear layer was similarly provided by a vortex sheet in isothermal conditions in Mancinelli *et al.* (2019a) because temperature and shear-layer-thickness effects coincidentally cancel out in the model.

The impact of the jet temperature ratio on the branch- and saddle-point locations is addressed in §C. We explore in the next section the improvements in the experimental data description that can be achieved by considering a flow model which takes into account the finite thickness of the shear layer of the jet.

4.1.2. Finite-thickness model

We first explore the shear-layer thickness effect on the definition of the St -band of existence of propagative k_p^- modes. We point out that no difference in the location of the branch and saddle points was observed between the vortex sheet and the finite-thickness dispersion relations for shear layers with $R/\theta_R \geq 30$, as large values of R/θ_R correspond to the V-S model. Figure 9 shows the branch- and saddle-point tracks in the M_j - St

Resonance tone	m	n of k_p^-	T	s	ϕ	p
A1	0	2	$\neq 1$	4	$-\pi/4$	3
A2	0	2	$\neq 1$	4	$-\pi/4$	4
TM	0	1	$\neq 1$	4	$-\pi/4$	2

TABLE 1. Summary of the parameters adopted to make resonance-frequency predictions using the vortex sheet.

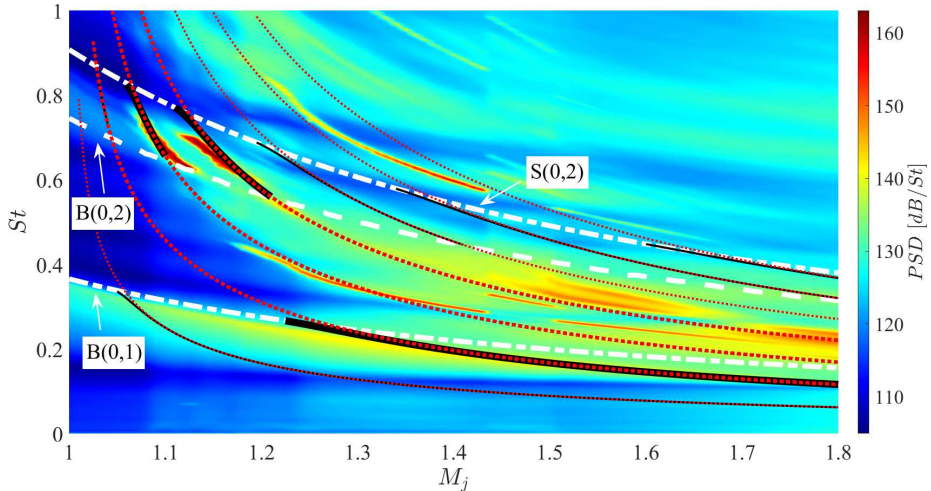


FIGURE 8. PSD map of mode $m = 0$ for a cold jet and predictions from neutral-mode analysis using the vortex sheet. Dotted red lines refer to predictions obtained using k_a^- waves, solid black lines to predictions obtained using k_p^- modes for $n = 1, 2$. Dashed and dash-dotted white lines correspond to the branch- and saddle-point tracks, respectively. Predictions for TM, A1 and A2 tones are represented with bold lines.

plane for different values of the shear-layer thickness. We choose thickness values with $R/\theta_R = 30, 20, 10$ and 5 and consider a cold jet in the model. The increase of the shear-layer thickness changes significantly the St -band of existence of the propagative guided mode of second radial order. Specifically, both the branch- and saddle-point tracks move to lower St when the shear-layer thickness increases and this shift is not linearly progressive but becomes increasingly more important as R/θ_R moves away from the value of 30. The shift towards lower St is more evident for $B(0,2)$ than for $S(0,2)$. Indeed, the shear-layer thickness effect on the saddle-point location appears to show a Mach-number dependence, with the shift towards lower St much more important for increasing M_j . The features just described result in a wider St -band of existence of k_p^- mode for $n = 2$ when the shear layer is thicker. We finally point out that no significant effect of the variation of R/θ_R is observed on the saddle point location of k_p^- mode of the first radial order.

It is thus clear that the thickness of the shear layer is an important parameter in the definition of the k_p^- modes and may strongly affect the accuracy of the screech-frequency prediction for modes A1 and A2. As detailed in §A, consistent with the results obtained from PIV data, we select $R/\theta_R = 10$.

Figure 10 shows the PSD map of $m = 0$ as a function of St and M_j and the screech-frequency predictions obtained using the guided modes as closure mechanism and considering a cold jet and a shear layer with $R/\theta_R = 10$. Branch- and saddle-point tracks

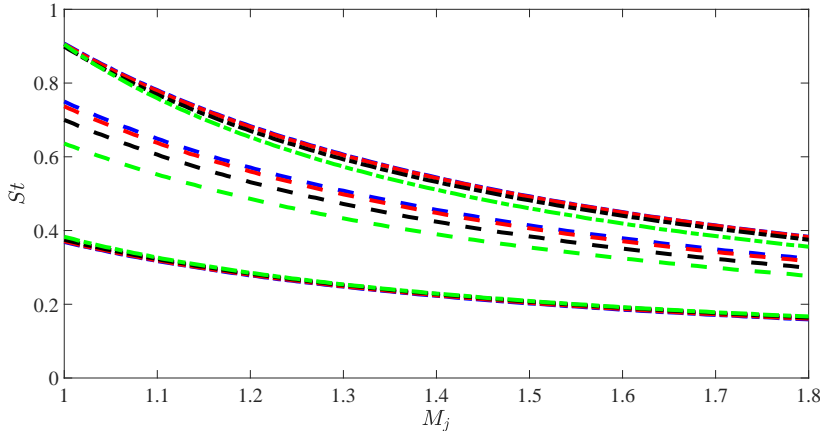


FIGURE 9. Branch- and saddle-point tracks of guided modes of first and second radial order for a cold jet and for different shear-layer thickness values. Dash-dotted lines refer to the saddle point, dashed lines to the branch point. Blue lines correspond to shear layer with $R/\theta_R = 30$, red lines to $R/\theta_R = 20$, black lines to $R/\theta_R = 10$, green lines to $R/\theta_R = 5$.

Resonance tone	m	n of k_p^-	R/θ_R	T	s	ϕ	p
A1	0	2	10	$\neq 1$	4	0	3
A2	0	2	10	$\neq 1$	4	0	4
TM	0	1	10	$\neq 1$	4	0	2

TABLE 2. Summary of the parameters adopted to make resonance-frequency predictions using a finite-thickness model in the case of a cold jet.

are also included in the plot. As outlined in §2.3, in-phase reflection conditions provided the best agreement with the experimental data. The list of parameters used to obtain screech-frequency predictions using a finite-thickness dispersion relation are summarised in table 2. In contrast to the V-S dispersion relation, both A1 and A2 screech modes are now entirely bounded by the branch- and saddle-point tracks. Predictions show a remarkable agreement with the experimental data for all screech modes A1, A2 and TM. Specifically, the accuracy of the prediction of the TM mode is strongly improved in comparison to that obtained using the vortex sheet: the mode is now accurately predicted in the range $M_j = [1.1, 1.8]$ against the range $M_j = [1.25, 1.8]$ obtained using the V-S model.

Nonetheless, as observed in the case of the vortex sheet, inaccuracies persist in the form of multiple tone predictions which do not correspond to measured tones: the model predicts tones for all the values of p considered in (2.14a). This represents a limitation of the neutral-mode model. In the next section we explore the improvements that can be obtained by considering the complex-mode resonance conditions using the finite-thickness dispersion relation to describe the jet-wave dynamics.

4.2. Complex-mode analysis

Figure 11 shows $m = 0$ PSD maps and predictions obtained using the complex-mode resonance conditions. Predictions are obtained varying p in eq. (2.14a) from 1 to 7

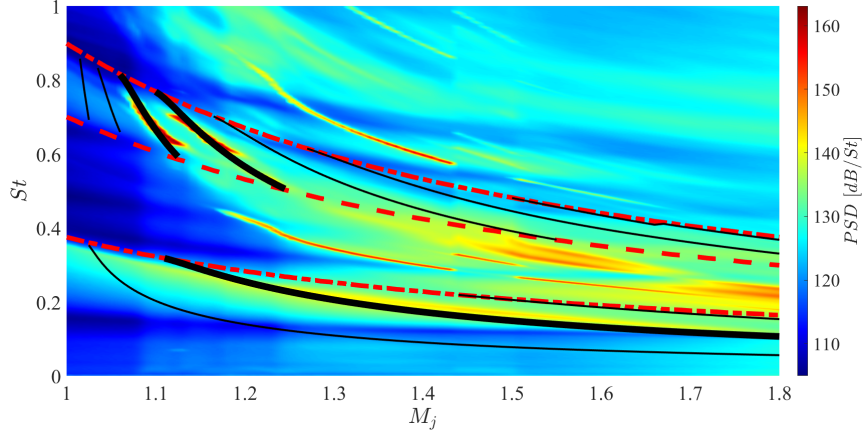


FIGURE 10. PSD map of mode $m = 0$ and screech-frequency predictions obtained from neutral-mode analysis using k_p^- modes for $n = 1, 2$ and considering a cold jet with $R/\theta_R = 10$. Bold black lines correspond to predictions of modes A1, A2 and TM. Dashed and dash-dotted red lines correspond to the branch- and saddle-point tracks, respectively.

and considering the same parameters listed in table 2. The threshold frequencies ω_r for which $\omega_i = 0$ for all M_j are also shown. These cut-off/cut-on frequencies define M_j - St regions for which $\omega_i \geq 0$, where screech resonance may thus be sustained. Predictions can be obtained only within this region, and the extent of this region in the M_j - St plane is a function of the amplitude of the reflection-coefficient product. We first explore four constant values of the reflection-coefficient product amplitude, $|R_1R_2| = 5 \cdot 10^{-2}$, 10^{-1} , $2 \cdot 10^{-1}$ and $3 \cdot 10^{-1}$. We observe that for $|R_1R_2| = 5 \cdot 10^{-2}$ the $\omega_r|_{\omega_i=0}$ contours appear only for k_p^- of second radial order and do not enclose any measured tones. As we increase the amplitude of the reflection-coefficient product, the region of positive imaginary frequencies extends to incorporate a broader M_j - St region, allowable resonance regions appear and predictions of A2, A1 and TM modes gradually emerge. Specifically, the agreement between the resonance predictions of both A1 and A2 modes and the experimental data appears satisfactory for $|R_1R_2| = 3 \cdot 10^{-1}$, whereas the TM mode is well-predicted only in the range $M_j = [1.1, 1.6]$. Spurious tone predictions are still observed for both $n = 1$ and $n = 2$ and these inaccuracies can be attributed to the crudeness of the reflection-coefficient product model.

The results shown above suggest a frequency-Mach-number-dependence of the amplitude of the reflection-coefficient product that must be considered in order to improve the accuracy of the resonance-prediction model.

4.2.1. Real-frequency model for reflection-coefficient identification

With a view to improving the reflection-coefficient model, we use a variant of the complex-mode model to perform a data-driven identification of the reflection-coefficient product. This approach aims at finding a functional form for the amplitude of the reflection-coefficient product to guide the complex-mode resonance model. We consider K-H and guided jet waves for $\omega \in \mathcal{R}$, in which case $k_{KH}^+ \in \mathcal{C}$ and $k_p^- \in \mathcal{R}$. For frequency-Mach number combinations for which tones are observed, we compute eigenvalues associated with these frequencies using the Rayleigh equation (2.5) and use the resonance condition in (2.7), $R_1R_2e^{i\Delta kL_s} = 1$, to calculate $R_1R_2 \in \mathcal{C}$. This calculation provides the reflection-coefficient product for $\omega_i = 0$, which corresponds to a feedback loop that neither grows nor decays in time. In the framework of the linear model, this amounts to

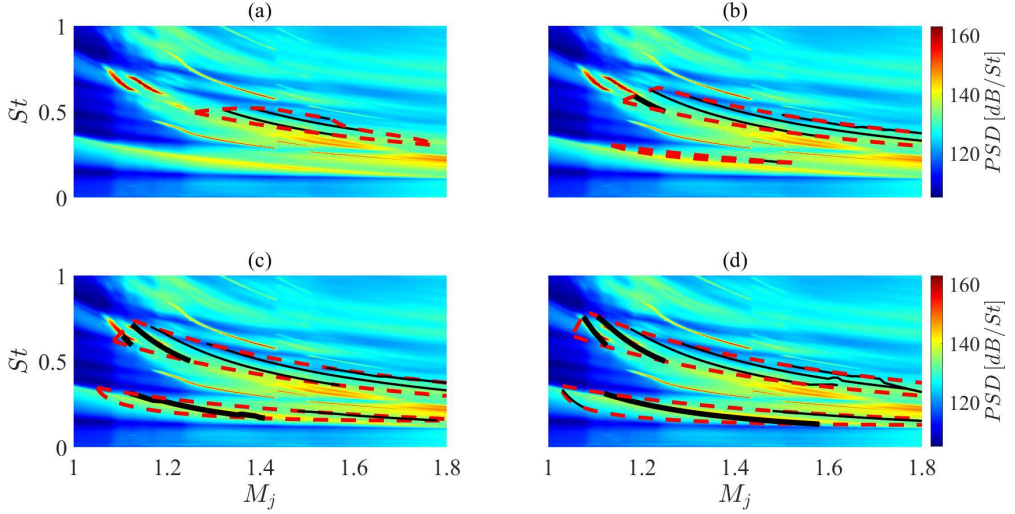


FIGURE 11. PSD maps of mode $m = 0$ and predictions from complex-frequency analysis for different amplitude values of the reflection-coefficient product: (a) $|R_1R_2| = 5 \cdot 10^{-2}$, (b) $|R_1R_2| = 10^{-1}$, (c) $|R_1R_2| = 2 \cdot 10^{-1}$, (d) $|R_1R_2| = 3 \cdot 10^{-1}$. Jet is considered cold with $R/\theta_R = 10$. Predictions for TM, A1 and A2 screech tones are represented with bold black lines, spurious predictions with solid black lines. The region of allowable resonances for which $\omega_i \geq 0$ is marked by dashed red lines.

the critical or minimum reflection-coefficient product necessary to sustain resonance and may be used as a first estimation to inform the full complex-mode model.

Figure 12 shows the amplitude of the computed critical reflection-coefficient product for the measured tone frequencies. The result confirms the order of magnitude of $|R_1R_2|$ used earlier but does not suggest a straightforward functional form of the frequency-Mach-number dependence. With the aim of keeping the functional form as simple as possible, we explore polynomial-surface fits and select a polynomial surface of the third degree along M_j and of second degree along St ,

$$|R_1R_2(St, M_j)| = \sum_{i=0}^3 \sum_{l=0}^2 c_{il} M_j^i St^l, \quad (4.1)$$

where the constants c_{il} are parameters determined via a least-mean-square-based fit of the critical $|R_1R_2|$ values in figure 12. The fitted model is shown in figure 13 and the new predictions in figure 14. Lines indicating $\omega_r|_{\omega_i=0}$ are also shown. We observe that the regions of allowable resonance frequencies for both $n = 1, 2$ are more tightly-fitted to the measured tones, the screech-frequency predictions are accurate and, more importantly, most of the spurious tone predictions have disappeared. Indeed, one spurious tone prediction is still observed for both $n = 1$ and $n = 2$. This could be likely ascribed to the limited amount of available data in the M_j - St domain to build the functional form of the reflection-coefficient product amplitude (see figure 12).

5. Conclusions

The resonance tones driven by axisymmetric azimuthal modes of a supersonic jet have been modelled. Attention was focused on the A1 and A2 screech modes and a low-frequency resonance peak, which we denoted TM, measured in the near pressure field of

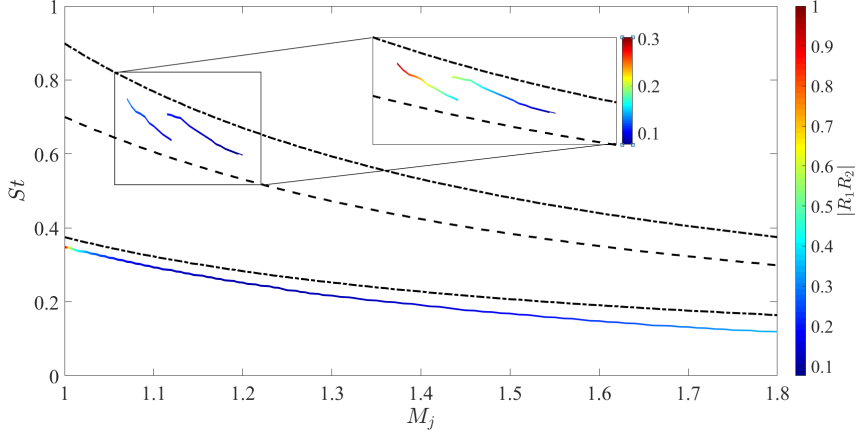


FIGURE 12. Representation of the critical or minimum amplitude of the reflection-coefficient product computed from eq. (2.7) considering $\omega \in \mathcal{R}$, $k_{KH}^+ \in \mathcal{C}$ and $k_p^- \in \mathcal{R}$ for azimuthal mode $m = 0$.

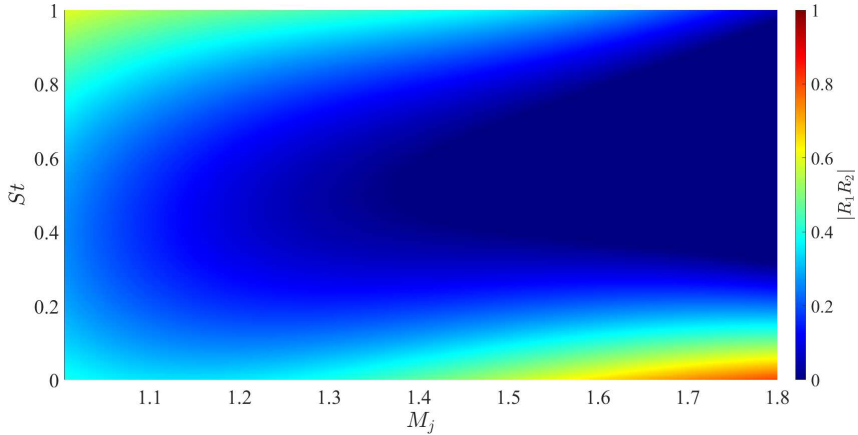


FIGURE 13. Representation of the semi-empirical shape of the reflection-coefficient product amplitude as a function of both St and M_j based on a polynomial-surface fit of the third and second degree along M_j and St , respectively, of the trend of the critical $|R_1R_2|$ reported in figure 12.

an under-expanded supersonic jet. The work follows our previous study (Mancinelli *et al.* 2019a), where we proposed a screech-frequency prediction model in which closure of the resonance loop is provided by upstream-travelling guided jet modes.

We here consider a resonance model that requires consideration of the upstream and downstream reflection coefficients, which appear in our model as the product R_1R_2 . We treat this as a parameter.

We first consider a model in which the frequency is real and both the downstream- and upstream-travelling waves are neutrally stable. This simplification allows us to neglect the amplitude of the reflection coefficients at the nozzle exit and shock-cell location. Resonance-frequency predictions are achieved just by imposing the phase of the reflection-coefficient product. We explore temperature and shear-layer thickness effects on the band of existence of propagative guided modes and, hence, on screech generation. We detail the limitations of the vortex sheet in describing the jet dynamics to accurately make screech-frequency predictions. We then explore the improvements obtained considering

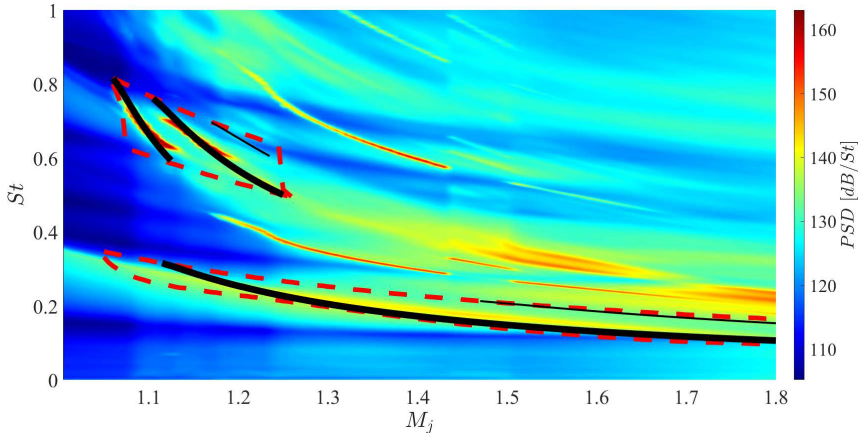


FIGURE 14. PSD map of mode $m = 0$ and resonance-frequency predictions obtained using a reflection-coefficient product amplitude function of both Strouhal and jet Mach numbers. Black lines correspond to predictions, dashed red lines delimit the region of allowable resonance frequencies, that is M_j - St region where $\omega_i \geq 0$.

a finite-thickness dispersion relation. Comparison with experimental data show how the predictions obtained considering a cold jet with a finite thickness value of the shear layer consistent with that obtained from Particle Image Velocimetry measurements are much more accurate. Inaccuracies persist, however, in the form of allowable resonance areas and spurious predictions for Strouhal and Mach number regions where no tones are observed.

We thus propose a more complete model in which both frequency and wavenumber are complex. In this framework, the downstream- and upstream-travelling waves are spatially unstable and evanescent, respectively. Both magnitude and phase reflection conditions must be considered in order to perform screech-frequency prediction. Positive values of the imaginary frequency identify regions of the M_j - St plane where resonance may be sustained and predictions obtained. These regions depend on the amplitude of the reflection-coefficient product. We propose a frequency-Mach-number-dependent model for the reflection-coefficient product amplitude. The frequency-Mach-number-dependent functional form is obtained via a data-driven identification based on a real-frequency-based variant of the complex-mode model. The estimated functional form is then used to inform the full complex-mode model to predict screech tones. With this refinement, spurious tone predictions are almost completely removed and the model provides a more complete description of the experimental observations.

Future efforts should be addressed to the development of an analytical model to rigorously determine the downstream and upstream reflection coefficients at the nozzle exit and shock-cell location without any input from the data. This work is currently underway by the authors. The complex-mode model could be then used to provide screech-tone predictions.

Appendix A. Particle Image Velocimetry results

PIV measurements have been performed to provide a description of the mean velocity field. For the sake of brevity, we restrict the attention to the jet Mach numbers for which A1 and A2 screech tones are measured, that is $M_j = 1.08, 1.12, 1.16, 1.22$. Figure 15 shows the mean-velocity-field maps as a function of the axial and radial positions x and r , respectively. The velocity values are normalised by the fully expanded jet velocity

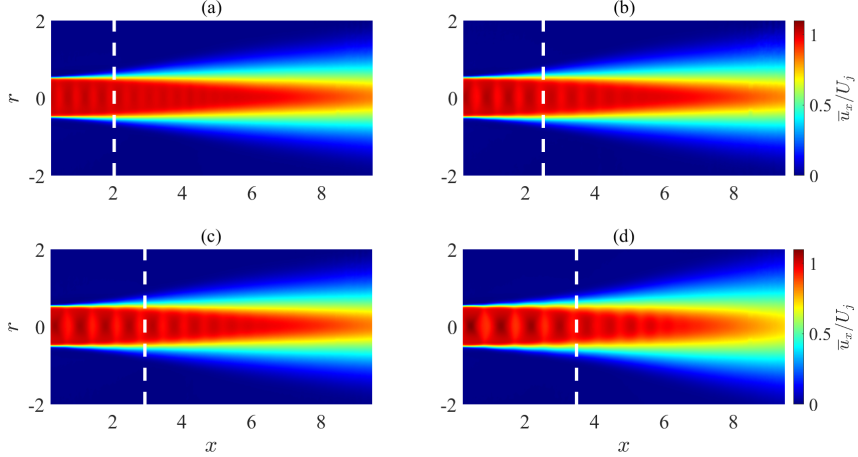


FIGURE 15. Mean velocity field obtained from PIV measurements for different jet Mach numbers: (a) $M_j = 1.08$, (b) $M_j = 1.12$, (c) $M_j = 1.16$, (d) $M_j = 1.22$. White dashed lines indicate the position of the downstream reflection point, that is the fourth shock cell, according to (2.9).

U_j and the positions of the downstream reflection points, that is the fourth shock cell, according to (2.9) are shown as well. We observe a good agreement between the shock reflection positions provided by the model and those measured by PIV. Specifically, the model slightly overestimates the axial location of the downstream reflection point but the discrepancy always stays under 10%.

As outlined in §2.1.2, PIV data have been used to estimate the shear-layer momentum thickness and thus calculate the hyperbolic-tangent velocity profile (2.6) to inform the finite-thickness model for the jet-dynamics description (2.5). Following Michalke (1984), the shear-layer momentum thickness for a compressible jet is computed as follows,

$$\theta_R = \int_0^\infty \frac{\bar{\rho}(r)}{\rho^*} \frac{\bar{u}_x(r)}{U^*} \left(1 - \frac{\bar{u}_x(r)}{U^*} \right) dr, \quad (\text{A } 1)$$

where the superscript * was for the centreline values in the subsonic flow analysed by Michalke (1984). We remind that the centreline velocity corresponds to the maximum velocity in the radial direction for a subsonic jet, which is not the case for a shock-containing supersonic jet as the one here analysed. We, hence, choose to use the superscript * to denote the position for which the maximum mean velocity value is detected in the radial direction. The mean density profile $\bar{\rho}(r)$ is obtained as the inverse of the temperature profile, $\bar{\rho}(r)/\rho_j = (\bar{T}(r)/T_j)^{-1}$, with the mean temperature computed from the mean velocity using Crocco-Busemann relation (Michalke 1984),

$$\frac{\bar{T}(r)}{T_j} = \frac{T_0}{T_j} + \left(1 - \frac{T_0}{T_j} \right) \frac{\bar{u}_x(r)}{U_j} + (\gamma - 1) M_j^2 \frac{\bar{u}_x(r)}{U_j} \frac{1}{2} \left(1 - \frac{\bar{u}_x(r)}{U_j} \right), \quad (\text{A } 2)$$

where T_0 is the stagnation temperature and U_j the fully-expanded jet velocity. Figure 16 shows the streamwise evolution of the ratio R/θ_R for the jet Mach numbers $M_j = 1.08$, 1.12, 1.16 and 1.22. The location of the downstream reflection point is reported as well. As expected, the R/θ_R value decreases with increasing axial distance. Specifically, its value varies in the range [6, 18] from the nozzle exit to the downstream reflection location. With the aim of keeping the model as simple as possible, we choose to use a unique

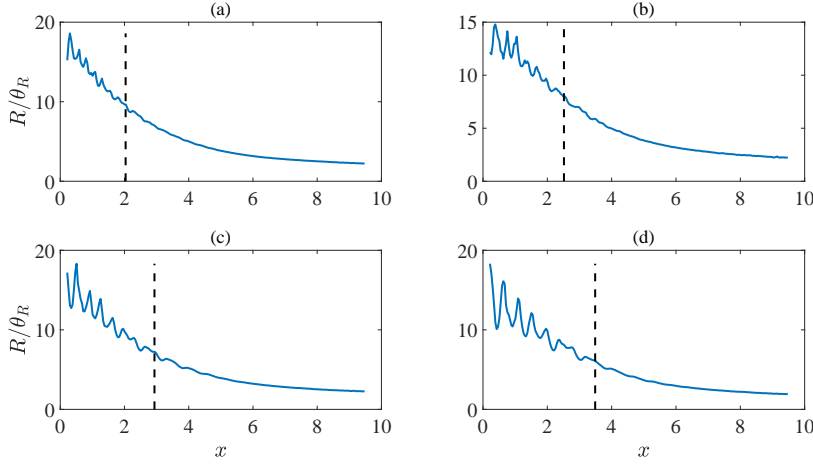


FIGURE 16. Streamwise evolution of R/θ_R , with θ_R the shear-layer momentum thickness, computed from the PIV mean velocity data for different jet Mach numbers: (a) $M_j = 1.08$, (b) $M_j = 1.12$, (c) $M_j = 1.16$, (d) $M_j = 1.22$. Black dashed lines indicate the position of the downstream reflection point, that is the fourth shock cell, according to (2.9).

analytic velocity profile (2.6) and we select $R/\theta_R = 10$ as an approximate average value independent of both axial distance and jet Mach number.

Appendix B. Non-linear interaction between azimuthal modes

The appearance of the asymmetric B, C and D modes in the spectral content of mode $m = 0$ due to non-linear interaction between modes $m = 1$ and $m = -1$ is proved by computing the cross-bicoherence between these azimuthal modes. Non-linear quadratic interaction between azimuthal modes occurs when $m_1 + m_{-1} - m_0 = 0$. Accordingly, the cross-bispectrum is computed as follows (Panickar *et al.* 2005),

$$B_c(f, m_1, m_{-1}, m_0) = \langle \hat{p}_1(f) \hat{p}_{-1}(f) \hat{p}_0^*(f) \rangle \quad (B1)$$

where $\hat{p}_m(f)$ is the Fourier transform of the m^{th} azimuthal mode, the superscript $*$ indicates complex conjugate and the symbol $\langle \cdot \rangle$ denotes ensemble average between 2048-element segments of the whole time series, thus leading to the same Strouhal number resolution of the *PSD* maps presented herein. A Hanning window and a 50% overlap are used to perform the bispectrum computation. The cross-bicoherence is obtained normalising the cross-bispectrum as follows,

$$b_c^2(f, m_1, m_{-1}, m_0) = \frac{|B_c(f, m_1, m_{-1}, m_0)|^2}{\langle |\hat{p}_0(f)|^2 \rangle \langle |\hat{p}_1(f) \hat{p}_{-1}(f)|^2 \rangle} \quad (B2)$$

Figure 17 shows the cross-bicoherence as a function of Strouhal number between azimuthal modes $m = 1$, $m = -1$ and $m = 0$ for $M_j = 1.3$. For this jet Mach number, only screech mode B is active and its signature should be found in $m = 1$ and $m = -1$ modes. We observe that a unitary bicoherence level is found for $St_1 = St_2 \approx 0.34$. This implies that a strong non-linear interaction occurs between modes $m = 1$ and $m = -1$ at $St \approx 0.34$ leading to the appearance of an energy signature in mode $m = 0$ for such frequency component, as confirmed by figure 7. We also observe low bicoherence levels along vertical and horizontal lines corresponding to the main screech frequency

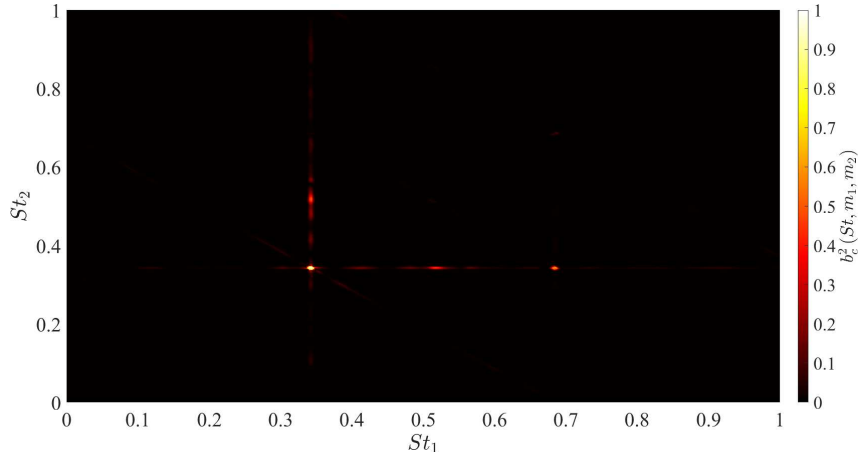


FIGURE 17. Cross-bicoherence between azimuthal modes $m = 1$, $m = -1$ and $m = 0$ for jet Mach number $M_j = 1.3$.

$St_1 = St_2 \approx 0.34$, where the subscript 1 and 2 refer to azimuthal modes $m = 1$ and $m = -1$, respectively. These indicate negligible non-linear interactions between the main screech-frequency and all the other frequencies, with the exception of the interaction between the screech frequency and its first harmonic $St \approx 0.68$. The signature of this interaction is, indeed, detected by the appearance of the first harmonic of B screech mode in the $m = 0$ PSD map of figure 7.

Appendix C. Temperature effects

We here explore the temperature effects on the branch- and saddle-point location of guided modes. For the sake of conciseness, we only report the results obtained using the vortex sheet for the jet-dynamics description and we underline that the same behaviour was observed in the finite-thickness model as well. Figure 18 shows the branch- and saddle-point tracks of guided modes of $m = 0$ and $n = 1, 2$ in the M_j - St plane for jet-to-ambient temperature ratios $T = 1, 0.9, 0.8, 0.7$ and 0.65 . Both $B(0, n)$ and $S(0, n)$ tracks move to higher frequencies when the temperature decreases; this trend is more evident for the guided jet mode of second radial order than that of the first radial order. As outlined above, this behaviour explains why the vortex-sheet model in isothermal conditions that was used by Mancinelli *et al.* (2019a) provided a good description of the experimental data similar to that we here obtain using a finite-thickness model and considering a cold jet. Specifically, the shift towards lower frequencies of the branch- and saddle-point tracks due to the increase of temperature is coincidentally compensated by the shift towards higher frequencies due to the reduction of the shear-layer thickness.

Acknowledgments

The authors acknowledge the financial support of EU and Nouvelle-Aquitaine region under the program CPER-FEDER. M.M. acknowledges the support of Centre National d'Études Spatiales (CNES) under a post-doctoral grant. Damien Eysseric is acknowledged for the support provided for the PIV measurements.

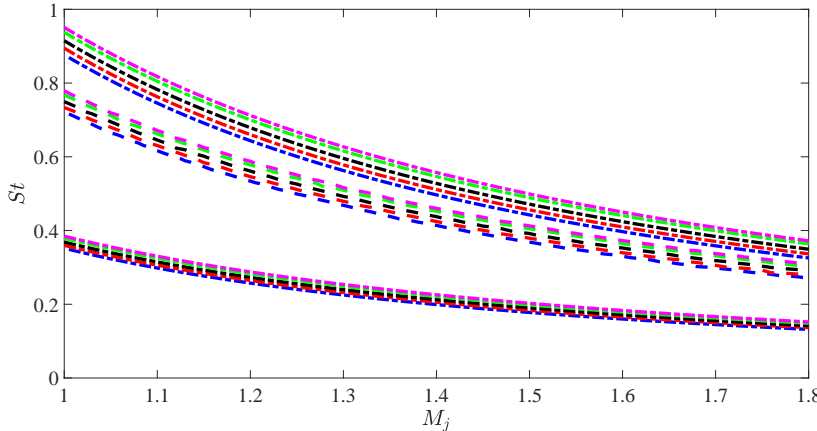


FIGURE 18. Branch- and saddle-point tracks of guided jet modes in the M_j - St plane for different jet-to-ambient temperature ratios T . Dash-dotted lines represent the saddle point, dashed lines the branch point. Blue lines refer to isothermal jet, i.e. $T = 1$, red lines $T = 0.9$, black lines $T = 0.8$, green lines $T = 0.7$, magenta lines to $T = 0.65$.

Declaration of Interests

The authors report no conflict of interest.

REFERENCES

BOGEY, C. & GOJON, R. 2017 Feedback loop and upwind-propagating waves in ideally expanded supersonic impinging round jets. *J. Fluid Mech.* **823**, 562–591.

CAVALIERI, A. V. G., JORDAN, P., COLONIUS, T. & GERVAIS, Y. 2012 Axisymmetric superdirective in subsonic jets. *J. Fluid Mech.* **704**, 388–420.

EDGINGTON-MITCHELL, D. 2019 Aeroacoustic resonance and self-excitation in screeching and impinging supersonic jets—a review. *Int. J. Aeroacoust.* **18**.

EDGINGTON-MITCHELL, D., JAUNET, V., JORDAN, P., TOWNE, A., SORIA, J. & HONNERY, D. 2018 Upstream-travelling acoustic jet modes as a closure mechanism for screech. *J. Fluid Mech.* **855**.

EDGINGTON-MITCHELL, D., OBERLEITHNER, K., HONNERY, D. R. & SORIA, J. 2014 Coherent structure and sound production in the helical mode of a screeching axisymmetric jet. *J. Fluid Mech.* **748**, 822–847.

GAO, JH & LI, XD 2010 A multi-mode screech frequency prediction formula for circular supersonic jets. *J. Acoust. Soc. Am.* **127** (3), 1251–1257.

GOJON, R., BOGEY, C. & MIHAESCU, M. 2018 Oscillation modes in screeching jets. *AIAA J.* **56** (7), 1–7.

HARPER-BOURNE, M. 1974 The noise from shock waves in supersonic jets—noise mechanism. *Agard Cp-131* **11**, 1–13.

JORDAN, P., JAUNET, V., TOWNE, A., CAVALIERI, A. V. G., COLONIUS, T., SCHMIDT, O. & AGARWAL, A. 2018 Jet-flap interaction tones. *J. Fluid Mech.* **853**, 333–358.

LANDAU, L. D. & LIFSHITZ, E. M. 1958 *Statistical physics*. Pergamon.

LESSEN, M., FOX, J. A. & ZIEN, H. M. 1965 On the inviscid stability of the laminar mixing of two parallel streams of a compressible fluid. *J. Fluid Mech.* **23** (2), 355–367.

LESSHAFT, L. & HUERRE, P. 2007 Linear impulse response in hot round jets. *Phys. Fluids* **19** (2), 024102.

MANCINELLI, M., JAUNET, V., JORDAN, P. & TOWNE, A. 2019a Screech-tone prediction using upstream-travelling jet modes. *Exp. Fluids* **60** (1), 22.

MANCINELLI, M., JAUNET, V., JORDAN, P., TOWNE, A. & GIRARD, S. 2019b Reflection

coefficients and screech-tone prediction in supersonic jets. In *25th AIAA/CEAS Aeroacoustics Conference. AIAA paper 2522*.

MERCIER, B., CASTELAIN, T. & BAILLY, C. 2017 Experimental characterisation of the screech feedback loop in underexpanded round jets. *J. Fluid Mech.* **824**, 202–229.

MERLE, M. 1957 Nouvelles recherches sur les fréquences ultrasonores émises par les jets d'air. In *Ann. Télécommun.*, , vol. 12, pp. 424–426. Springer.

MICHALKE, A. 1970 A note on the spatial jet-instability of the compressible cylindrical vortex sheet. *Tech. Rep.*.. DLR.

MICHALKE, A. 1984 Survey on jet instability theory. *Prog. Aerosp. Sci.* **21**, 159–199.

NOBLE, B. 1958 *Methods based on the Wiener-Hopf technique for the solution of partial differential equations*. Pergamon Press London.

PACK, D. C. 1950 A note on prandtl's formula for the wave-length of a supersonic gas jet. *Q. J. Mech. Appl. Math.* **3** (2), 173–181.

PANDA, J. 1999 An experimental investigation of screech noise generation. *J. Fluid Mech.* **378**, 71–96.

PANICKAR, PRAVEEN, SRINIVASAN, K & RAMAN, GANESH 2005 Nonlinear interactions as precursors to mode jumps in resonant acoustics. *Phys. Fluids* **17** (9), 096103.

POWELL, A. 1953 On the mechanism of choked jet noise. In *Proc. Phys. Soc. London, Sec. B*, , vol. 66, p. 1039.

POWELL, A., UMEDA, Y. & ISHII, R. 1992 Observations of the oscillation modes of choked circular jets. *J. Acoust. Soc. Am.* **92** (5), 2823–2836.

RAMAN, GANESH 1999 Supersonic jet screech: half-century from powell to the present. *J. Sound Vib.* **225** (3), 543–571.

RIENSTRA, SJOERD W 2007 Acoustic scattering at a hard–soft lining transition in a flow duct. *J. Engrg Math.* **59** (4), 451–475.

SCHMIDT, O. T., TOWNE, A., COLONIUS, T., CAVALIERI, A. V. G., JORDAN, P. & BRÈS, G. A. 2017 Wavepackets and trapped acoustic modes in a turbulent jet: coherent structure eduction and global stability. *J. Fluid Mech.* **825**, 1153–1181.

SHEN, H. & TAM, C. K. W. 2002 Three-dimensional numerical simulation of the jet screech phenomenon. *AIAA J.* **40** (1), 33–41.

SORIA, J. 1996 An investigation of the near wake of a circular cylinder using a video-based digital cross-correlation particle image velocimetry technique. *Exp. Therm. Fluid Sci.* **12** (2), 221–233.

TAM, C. K. W. & AHUJA, K. K. 1990 Theoretical model of discrete tone generation by impinging jets. *J. Fluid Mech.* **214**, 67–87.

TAM, C. K. W. & HU, F. Q. 1989 On the three families of instability waves of high-speed jets. *J. Fluid Mech.* **201**, 447–483.

TAM, C. K. W., SEINER, J. M. & YU, J. C. 1986 Proposed relationship between broadband shock associated noise and screech tones. *J. Sound Vib.* **110** (2), 309–321.

TOWNE, A., CAVALIERI, A. V. G., JORDAN, P., COLONIUS, T., SCHMIDT, O., JAUNET, V. & BRÈS, G. A. 2017 Acoustic resonance in the potential core of subsonic jets. *J. Fluid Mech.* **825**, 1113–1152.

TREFETHEN, L. N. 2000 *Spectral methods in MATLAB*. SIAM.

WELCH, P. 1967 The use of fast fourier transform for the estimation of power spectra: a method based on time averaging over short, modified periodograms. *IEEE Trans. Audio Electroacoust.* **15** (2), 70–73.

WESTERWEEL, J. & SCARANO, F. 2005 Universal outlier detection for piv data. *Exp. Fluids* **39** (6), 1096–1100.

WILLERT, C. E. & GHARIB, M. 1991 Digital particle image velocimetry. *Exp. Fluids* **10** (4), 181–193.